Acta Materialia 256 (2023) 119095

Contents lists available at ScienceDirect

Acta Materialia

journal homepage: www.elsevier.com/locate/actamat

Full length article

# The microstructural origin of a hardness double-peak in an age-hardened EN-AW 6082

Christoph M. Hell [a,*], Bjørn Holmedal [b], Ruben Bjørge [c], Calin D. Marioara [c], Randi Holmestad [a]

[a] Department of Physics, Norwegian University of Science and Technology (NTNU), Trondheim N-7491, Norway
[b] Department of Materials Science and Engineering, NTNU, Trondheim N-7491, Norway
[c] SINTEF Industry, Trondheim N-7465, Norway

ARTICLE INFO

*Keywords:*
Age hardening
Double-Peak hardening
(Scanning) Transmission Electron Microscopy
6xxx
Strength modeling

ABSTRACT

In this study, the origin of a double-peak during artificial aging of an EN-AW 6082 is analyzed with (S)TEM. The acquired TEM data is used as an input into a strength model by Holmedal [1] to explore the origin of the double-peak, thus, a broader strength plateau. It is concluded that the first peak arises after about 160 min at 175 °C from a population of relatively wide $\beta''$-type precipitates with a high number density and a narrow length spread. The second peak occurs after 10 h artificial aging and can be traced to a broader size distribution of precipitate lengths of roughly the same type of precipitates as found for the first peak. The longest precipitates, however, act more efficiently as obstacles for gliding dislocations and maintain therefore the high strength. Those long precipitates are of a hybrid type of different, but mainly overaged phases. It is found that this broad strength plateau with a double-peak can arise after a rapid heat-up to the artificial aging temperature. Due to the rapid heat-up, structures of overaged phases are already found within the $\beta''$ precipitates of the first peak making them wider. Ultimately, however, this leads to the evolution of few but very large overaged hybrid-type precipitates co-existing with $\beta''$-type precipitates at the second peak. The mixed morphology counteracts the loss of strength from Ostwald ripening and leads to the second peak. A slower heating rate results in fewer precipitate nucleation sites and in the formation of longer and purer but slimmer $\beta''_{perfect}$ phases.

## 1. Introduction

Age hardening is a widely employed process to increase the strength in different material systems. In the case of aluminium alloys, age hardening is conducted for the high and medium-high strength alloys, typically of the 2xxx (Al–Cu), 6xxx (Al-Mg-Si(-Cu)) and 7xxx (Al-Mg-Zn) series. These alloys owe their strength to the formation of finely dispersed needle, lath or plate-like precipitates that form during the age-hardening process and their interaction with gliding dislocations. A typical age-hardening process consists of three main steps: (1) *Solutionizing* the precipitate-forming elements within the parental matrix; (2) *Quenching* to create a supersaturated solid-solution (SSSS) enriched with vacancies; (3) *Artificial-aging (AA)* to promote the precipitate formation [2]. However, the details of the several steps, e.g. the AA temperature, the cooling rate or eventual waiting between the solution heat treatment and AA treatment, can lead to significant changes in the AA response and a changed precipitate distribution [3,4]. In the case of the Cu-poor 6xxx system, different metastable precipitates might form during the course of the AA treatment until the equilibrium phases have formed. Those metastable precipitates are all oriented along the ⟨100⟩ Al direction and transform gradually from highly coherent ones to the incoherent but energetically stable equilibrium phases $\beta$ and Si. The sequence is commonly accepted as [2,3]:

$$\text{SSSS} \rightarrow \text{Clusters} \rightarrow \text{GP-zones} \rightarrow \beta'' \rightarrow \beta', B', U1, U2 \rightarrow \beta, \text{Si}$$

In the presence of Cu the alloy forms the stable Q- phase besides Si. Hence, the sequence changes to [2,5]:

$$\text{SSSS} \rightarrow \text{Clusters} \rightarrow \text{GP-zones} \rightarrow \beta'', L, C \rightarrow \beta'_{Cu}, Q' \rightarrow Q, \text{Si}$$

Age hardening leads to nucleation and growth of those precipitates which act as obstacles and restrict dislocation movement. The common understanding of the dislocation–precipitation interaction is based on dislocations shearing the precipitates or bypassing and leaving dislocation loops (Orowan mechanism). The shearing leads to modifications of the precipitate-matrix interface and creation of new internal interfaces by modification of the stacking in the precipitates, e.g. anti-phase boundaries. The dislocation loops create a stress field which exerts a

* Corresponding author.
*E-mail address:* christoph.hell@ntnu.no (C.M. Hell).

https://doi.org/10.1016/j.actamat.2023.119095
Received 2 March 2023; Received in revised form 31 May 2023; Accepted 14 June 2023
Available online 23 June 2023

**Table 1**
Alloy composition of the 6082.

| at. % | Si | Mg | Cu | Fe | Mn | Cr | Zn | Ti | Zr | V | B | Al |
|---|---|---|---|---|---|---|---|---|---|---|---|---|
| 6082 | 0.878 | 0.725 | 0.004 | 0.102 | 0.257 | 0.083 | 0.025 | 0.011 | – | 0.011 | 0.010 | 97.894 |

back stress on succeeding dislocations which in turn need a higher stress to pass the obstacle [6]. In both cases, the precipitates act as dislocation obstacles and increase the strength, hence, the resulting hardness of the alloy.

During the initial stages of the aging process the obstacle strength contributed from each particle increases with increasing precipitate size. The precipitates formed in the here considered alloy exhibit large aspect ratios, thus their obstacle strength increases with their cross section until they reach a critical area which can no longer be sheared by the dislocations. From this point on, the energetically most favorable option for a dislocation to pass is by looping [6,7]. Thus, further increase of the precipitate cross section will not increase the obstacle strength. Note, however, that a further increase of the precipitate length, will make it pierce a higher number of slip planes and by that contribute to more precipitate-based dislocation obstacles per slip plane. At some point during aging, the solute level in the matrix runs low and coarsening through Ostwald ripening sets in. Solute atoms have on average a higher chemical potential at the vicinity of smaller particles, thus, the smallest particles will dissolve, while the largest will grow [6,8]. The largest particles are then usually thick enough to act as strong obstacles. But the decrease of the number density of precipitates during coarsening will make the alloy softer.

Therefore, as the alloy experiences age hardening, its strength will increase in the underaged state until it eventually reaches its peak strength. Further aging will put the alloy in an overaged state accompanied by a loss of strength. Consequently, a single peak of strength appears.

A double-peak aging behavior has been observed and described in the literature for several age hardenable material systems which form high aspect ratio precipitates, such as in maraging steels [9] and in several different aluminium series, e.g. 2xxx [10], 6xxx [3,11], 7xxx [12] or Al–Si cast alloys [13]. In a recent study we showed that the heat-up rate to AA temperature can have a significant effect on the peak-strength plateau of two different 6xxx alloys [14]. In that study, an EN-AW 6082 (6082) and a Cu containing EN-AW 6110 (6110) alloy showed a broader peak-strength plateau when a quick heat-up rate was used. Heating the alloys slowly up (ramping) to the AA temperature resulted in a shorter strength plateau. For the 6082 the strength plateau was longer by about two hours due to a pronounced double-peak. In the present study the origin of the double-peak in the hardness curves is investigated on the basis of precipitate statistics acquired through (scanning) transmission electron microscopy ((S)TEM) of the same alloy aged with and without ramping up to the AA temperature. The acquired TEM results are then used as an input into a strength model [1] to explore the origin of the double-peak.

## 2. Experimental

### 2.1. Material, method and precipitate quantification

An extruded 6 mm thick profile of 6082 was cut into 20 × 35 × 6 mm rectangular samples. The alloy composition can be found in Table 1. The samples were ground down to 4000 grit with a *Struers Rotopol 60*. The 45 min solution heat treatment and AA was conducted at 525 °C in a preheated *Nabertherm Forced Convection Chamber Furnace NA 15/65* and at 175 °C ± 0.5 in a preheated *Memmert Oilbath*, respectively. Quenching was done directly into 20 °C ± 5 cold water. The ramp to AA temperature was done with a heating rate of 0.02 $\frac{K}{s}$ in a *Nabertherm Forced Convection Chamber Furnace NA 17/HR* starting from 20 °C.

The heat treatment without a ramp is referred to as *dAA*. The heat treatment with a temperature ramp to AA temperature is referred to as *rAA*. The AA times for the two analyzed conditions are given in Table 2. The Vickers hardness (HV) development during AA was tracked on individual samples with 10 indents on an *Innovatest Vickers hardness testing machine* with a dwell time of 10 s and a load of 1 kgf.

(S)TEM samples were prepared by electropolishing in a *Struers Tenupol-5* electropolishing unit. The electrolyte was a 2:1 methanol, nitric acid mixture. TEM bright field (BF) and dark field (DF) investigations were done with *Jeol JEM 2100* at an acceleration voltage of 200 keV and a condenser aperture of 70 µm in [001] zone axis. The high resolution TEM (HRTEM) images were acquired with a 20 µm objective lens aperture. Micrographs were recorded with a *Gatan 2k Orius CCD* camera. STEM investigations were carried out on a *Jeol JEM ARM200F*, double corrected (S)TEM with a cold field emission gun. A condenser aperture of 40 µm, corresponding to a semi-convergence angle of 27 mrad and a Gatan detector with inner and outer collection angles of 51–203 mrad for high-angle annular dark field (HAADF) recordings was used. Presented images were scan-distortion corrected by the acquisition of 20–24 individual scans with a 90° scan rotation between each. The images were then created by a subsequent rigid image registration routine and averaging over the aligned micrographs [15]. An exact description of the sample preparation and (S)TEM setup can be found elsewhere [14].

*Precipitate quantification*

(S)TEM investigations were performed on individual grains which did not require tilting of more than 6° to [001] zone axis. A set of BF images with a magnification of 120 k, DF micrographs with 200 k and {220} 2-beam convergent-beam electron diffraction (CBED) patterns were taken. The average length $l_{mean}$ of the precipitates was measured from all distinguishable precipitates from two BF images per analyzed condition. The mean precipitate number density $\rho_{mean}$ was acquired from five different DF images and calculated per image by:

$$\rho = \frac{3N}{At\left(1 + \frac{l_{mean}}{t}\right)} \tag{1}$$

with $N$ being the number of counted precipitates aligned parallel to the optical axis and $A$ being the image area. The thickness $t$ was determined from CBED patterns for each DF image [16]. By fitting parallelograms to the precipitates from the HRTEM micrographs, taken with a magnification of ≥ 1.2 M, the mean precipitate cross sectional area $a_{mean}$ was found. The mean volume fraction $f_V$ is estimated on the basis of five different precipitate number densities through: $f_V = \rho \cdot a_{mean} \cdot l_{mean}$. The errors given are expressed as the standard deviation for $l_{mean}$, $\rho_{mean}$ and $f_V$. The standard error marks the deviation of $a_{mean}$. The value $l_{Peak}$ describes the precipitate length with the highest occurring frequency in each length distribution $\phi$.

Precipitate types were categorized from HAADF-STEM micrographs taken within the bulk of grains. Thus, precipitates emerging from dispersoids or apparent dislocations were omitted. Fig. 1 displays example images of precipitates with their unit cells and characteristic building blocks of different categories used for precipitate type characterization. Precipitates referred to as hybrid show building blocks of different metastable precipitates. It has to be mentioned that only indirect conclusions of the relation of precipitate types and precipitate lengths can be drawn. This is, because for imaging precipitate lengths, the precipitates have to be orthogonally aligned to the optical axis. Whereas to image the precipitate cross sectional area or type, the precipitates have to lie parallel to the optical axis.

**Table 2**
AA times with and without temperature ramping.

| AA times | | | | | | | | | | | |
|---|---|---|---|---|---|---|---|---|---|---|---|
| dAA | As-quenched | 10 min | 20 min | 40 min | 80 min | 160 min | 5 h | 10 h | 25 h | 3 d | 7 d |
| rAA | After ramp | 10 min | 20 min | 40 min | 80 min | 160 min | 5 h | 10 h | 24.25 h | 3 d | 7 d |

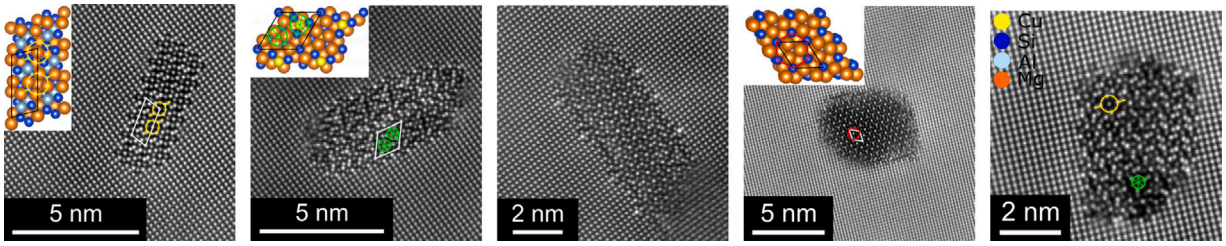


(a) $\beta''$ (b) $B'$ (c) $L$ (d) $\beta'$ (e) $\beta''_{Hybrid}$

**Fig. 1.** HAADF-STEM micrographs of metastable phases of the five different categories used in this work. Each micrograph is the average of 24 individual scans. When present, the unit cell of the different phases is depicted, as well as their repeating building block. Images (a), (b) and (c) were taken after 10 h from the dAA treatment and (d) and (e) from the rAA treatment after 24.25 h AA.

### 2.2. Strength modeling

The strength of the material stems from obstacles to dislocation glide. The most important obstacles in the 6xxx system are precipitates, while stored dislocations, grain boundaries and atoms in solid solution add secondary contributions to strength [17]. The material texture will provide some anisotropy to the strength. These contributions to the critical resolved shear stress $\tau$ for dislocation glide are commonly linearly added [17], even though a quadratic mixing is strictly more adequate [18]. Adding the contributions linearly can, however, be justified when the dislocation density is relatively low and precipitates provide much more dislocation pinning points, compared to forest dislocations:

$$\tau = \tau_0 + \tau_{ss} + \tau_d + \tau_p \tag{2}$$

with solid-solution strengthening $\tau_{ss}$, a contribution from stored dislocations $\tau_d$ and a contribution of precipitates $\tau_p$ superimposed to all other contributions $\tau_0$. The strength model from [1] allows an estimation of the particle contribution to the strength $\tau_p$ on the basis of precipitate size distributions $\phi$ acquired by TEM. In the following, a short introduction is given. The reader is, however, referred to the original paper by Holmedal [1] and the refined version to account for multi-modal precipitate size distributions and work-hardening by Lu et al. [19]. The strength model is based on three assumptions:

1. The cross-sectional area, $a$, of a precipitate is constant along its length $l$.
2. The dimensionless obstacle strength $f$ of an individual precipitate towards a gliding dislocation is only given by its $a$ and therefore constant throughout $l$.
3. A relation between the cross sectional area $a$ and length $l$, i.e., the aspect ratio ($\Omega$), exists [20].

The last assumption allows us to simplify the model. Instead of taking the two two-dimensional precipitate size distributions of $l$ and of $a$ into account, one finds an expression for the aspect ratio $\Omega$ as a function of $l$ and has to deal with only one size distribution:

$$\Omega = \frac{l}{\sqrt{a}} = \max\left(c \cdot l^m, 1\right) \tag{3}$$

with $c$ and $m$ being parameters that need to be fitted to the relation between $a_{mean}$ and $l_{mean}$, which were experimentally determined from different aging times.

The second assumption allows us to find an expression for the normalized obstacle strength $f$ of individual precipitates. The obstacle strength $f$ is maximum for non-shearable precipitates with large $a$, for which $f = 1$. The transition between looping and shearing is defined by a critical cross section $a_c$. The numerical value for the obstacle-strength $f$ is determined by:

$$f = \min\left(\left(\frac{a}{a_c}\right)^{\kappa}, 1\right) \tag{4}$$

with the empirical parameter $\kappa$. The parameter $\kappa$ describes how the pinning force of shearable precipitates evolves with their growing cross-section. In this work we assume that the pinning force is directly related to the cross-section, hence $\kappa = 1$, as in [1]. However, one might also suggest that the change of the pinning force is rather governed by the radius of the cross-section, in that case one chooses $\kappa = \frac{1}{2}$ [21]. It cannot be said at which cross section size $a_c$ the transition from shearing to looping occurs and its value is often chosen case specific. Some studies suggest that this might happen in the slightly overaged regime [22]. However, we assume in this work that $a_c$ is encountered early at peak strength. Since $\Omega$ links the values of $a$ with $l$, $f$ can also be expressed in terms of lengths:

$$f = \min\left(\left(\frac{l^2}{\Omega^2 a_c}\right)^{\kappa}, 1\right) \tag{5}$$

Therefore, the strength contribution $\tau_p$ depends on a given measured precipitate length distribution $\phi_l$ and its resulting mean obstacle strength $\bar{f}$. The strength contribution $\tau_p$ is estimated on the basis of the line-tension simulations by De Vaucorbeil et al. [23]:

$$\tau_p = \alpha_p G b \sqrt{n_p} \bar{f}^{\frac{3}{2}} \cdot \left(1 - \frac{1}{6}\bar{f}^5\right) \tag{6}$$

with $\alpha_p$ being a constant for scaling purpose, $b$ the Burger's vector, $G$ being the shear modulus and the mean obstacle strength $\bar{f}$. De Vaucorbeil et al. [23] showed that the expression of $\tau_p$ gives a lower bond estimate when all the particles exert the same pinning strength on the gliding dislocations. However, they showed, as well, that this lower bond estimate lies within a small error range when $\bar{f} \geq 0.8$ for most size distributions typically encountered.

The equivalent stress of a tensile test can be found as $\sigma = M\tau$, where the Taylor factor $M$ accounts for the texture induced anisotropy. Due to the large aspect ratio of the precipitates commonly found in the 6xxx system, the elongated precipitates act as dislocation obstacles on numerous slip planes, which is expressed by the number density of precipitate-based obstacles per slip plane $n_p$. The estimation of $n_p$ is based on the consideration that ⟨100⟩ oriented precipitates act as obstacles on any {111} gliding plane within their reach. The value of $n_p$ can then be estimated through:

$$n_p = \frac{\sqrt{3}}{3} l_{mean} \cdot \rho_{mean} \tag{7}$$

with $\cos\alpha = \sqrt{3}/3$ being the angle between the aforementioned main precipitate growth direction and the glide-plane normal. A thorough explanation of the derivation of this relation is given in the original article by Holmedal [1].

The mean obstacle strength $\bar{f}$ needs to be numerically determined and depends amongst others on the precipitate length distribution $\phi_l$:

$$\bar{f} = \frac{\int_0^\infty f l \phi_l dl}{\int_0^\infty l \phi_l dl} = \left( \frac{1}{a_c^\kappa} \int_0^{\Omega_c \sqrt{a_c}} \frac{l^{2\kappa+1}}{\Omega (l)^{2\kappa}} \phi_l dl + \int_{\Omega_c \sqrt{a_c}}^\infty l \phi_l dl \right) \frac{1}{l_{mean} \rho_{mean}} \tag{8}$$

The first term relates to shearing, whereas the second term expresses the looping behavior.

The normalized precipitate length distribution $\phi_l$ is represented by a kernel density estimator with a Gaussian kernel to account for multi-modal distributions [19]. This is done in a two-step process. In a first step, an uncorrected distribution $\tilde{\phi}$ is calculated over all measured needle lengths $N_l$:

$$\tilde{\phi} = \frac{1}{N_l} \sum_{i=1}^{N_l} \frac{\sqrt{2} \exp\left( -\frac{1}{2} (\frac{l - l_i}{h})^2 \right)}{\left( 1 + \mathrm{erf}(\frac{l_i}{\sqrt{2} h}) \right) h \sqrt{\pi}} \tag{9}$$

with $h$ being the bandwidth, assessed through Scott's rule: $h \approx d N_l^{-0.2} \sigma_l$ and $\sigma_l$ being the standard deviation of the length distribution and $d = 0.8$. Since the precipitate length distribution is a bounded domain, i.e. the length distribution $\phi_l$ needs to reach the value 0 for $l = 0$, a kernel is centered on $l = 0$ and subtracted from $\tilde{\phi}$ in a second step:

$$\phi = \frac{\tilde{\phi} - \tilde{\phi}(0) \exp\left( -\frac{1}{2} (\frac{l}{h})^2 \right)}{1 - \frac{1}{2} h \sqrt{2\pi} \tilde{\phi}(0)}, \; l \geq 0 \tag{10}$$

The experimental results of the TEM measurements will be used as input to see if the double-peak is represented in the acquired precipitate data. By comparing in a second step the parameters of the different conditions, i.e. $n_p$, $l_c$ and $\bar{f}$, conclusions on the microstructural origin of the double-peak can be drawn. Since the main gain in strength stems from precipitates [17], we mainly concentrate on their contribution to the double-peak in the hardness curves.

## 3. Results

### 3.1. Hardness curves

Fig. 2 displays the AA responses of the 6082 alloy during isothermal aging at 175 °C for the heat treatments labeled "dAA" and "rAA", corresponding to without and with ramping up to the AA temperature, respectively. A clear double-peak in the age hardening curve can be seen on the strength plateau of the dAA treatment without the ramping. The first peak occurs after 160 min of AA. After 5 h of AA a decrease of hardness occurs. However, 10 h of AA leads to another hardness peak. On the other hand, with ramping up to the AA temperature, the hardness curve does not show any double-peak. Instead, the material reaches delayed about the same maximum hardness and overages subsequent to reaching it. In the supplementary hardness data for heat treatments with varying amount of natural aging, i.e. holding time at room temperature prior to AA, are shown. The double peak is clearly seen in the additional heat treatment routs of the dAA treatment, wheres the rAA treatment only produced a single peak regardless of the NA time. Tensile test data from another similar 6082 are presented in the supplementary, as well. The tensile data of the other 6082 do not show a double-peak. However, the tensile data show clearly the broader strength plateau of the dAA treatment compared to the narrow one of the rAA treatment.

To apply the strength model, the hardness values are converted into yield strength values which will be used to calibrate and compare

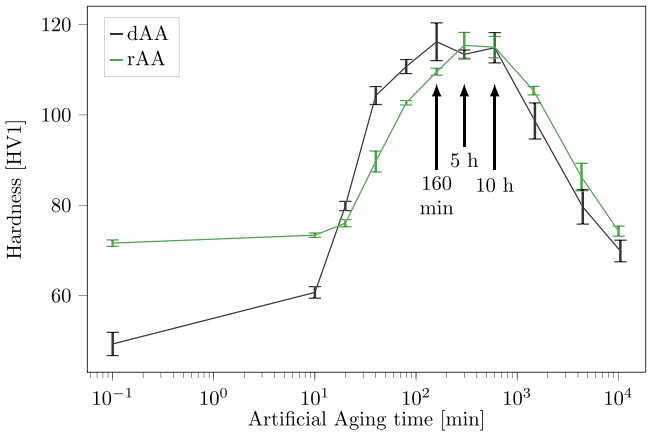


**Fig. 2.** Hardness curves of the 6082 alloy during AA at 175 °C without ramping directly after quenching (dAA), and AA after a 2 h ramp to AA temperature (rAA).

the modeled values. As a rule of thumb the relation between hardness values HV and the yield strength $R_p$ can be approximated through $R_p \approx 3 \cdot HV$ [17,24–28]. As shown in the work of Lu et al. [19], the ability for work hardening is strongly reduced and very similar around the strength plateau and for the here investigated AA times for this type of alloy. Hence the conversion factor from HV to $R_p$ for the three analyzed conditions can be assumed as constant. Table 3 shows the three hardness values of the two analyzed heat treatments and the expected $R_p$ values.

### 3.2. Precipitate statistics

Lengths of the precipitates were quantified based on BF images. Examples of those BF images are shown in Fig. 3 for the dAA treatment and in Fig. 5 for the rAA treatment. About 600 needles or more were measured per condition. Cross-sectional areas of the precipitates were measured from HRTEM micrographs. Kernel density estimates were applied through Eqs. (9) and (10) from those measurements to estimate the corresponding size distribution. The size distributions displayed through the classical bar-plot can be found in the supplementary. Fig. 4 shows the precipitate length and cross-sectional area distributions of the dAA treatment and Fig. 6 shows the distributions of the rAA treatment. The precipitate type statistics of the six analyzed conditions are given in Table 4 and the summarized precipitate statistics of all investigated conditions are given in Table 5.

Compared to the dAA treatment, the rAA treatment produces significantly longer but slimmer precipitates and significantly fewer of them at all investigated aging times, as seen in Table 5. The precipitate type analysis shows for all analyzed conditions of the rAA treatment a higher occurrence of $\beta''_{perfect}$ precipitates, compared to the corresponding conditions for the dAA treatments.

### 3.3. Strength modeling

The strength due to age hardening $\tau_p$ was calculated with the length distributions $\phi_l$ from Figs. 4(a) and 6(a). The average length $l_{mean}$ and precipitate number density $\rho_{mean}$ are given in Table 5. The remaining values are given in Table 6. The Taylor factor M for random grain distribution was taken from Zhang et al. [29]. The $\alpha_p^{dAA}$ value was calibrated by matching the $\sigma_p$ value of the first peak, hence, after 160 min dAA to the corresponding $R_p = 348.6$ MPa. The rAA treatment was matched to the single peak after 5 h rAA, hence, to $R_p = 346.2$ MPa, see Table 3. The value of the critical cross section $a_c$ is assumed to occur early at peak strength, thus the smallest measured $a_{mean}$ found at peak strength is used in the calculations.

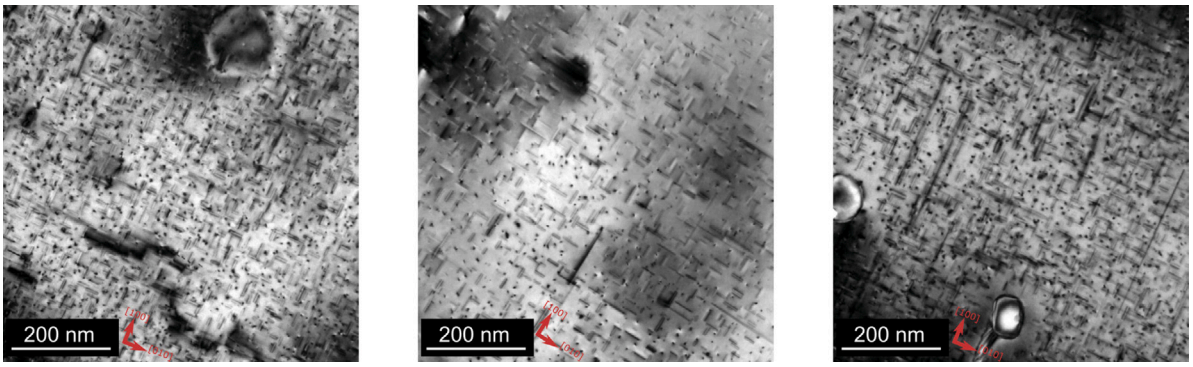


(a) 160 min (b) 5 h (c) 10 h

**Fig. 3.** One of the two images of the analyzed BF micrographs from each condition of the dAA treatment. The grains are [001] oriented and the measured thickness $t$ is given. (a) first peak (160 min AA), $t = 72.9$ nm; (b) between peaks (5 h AA), $t = 39.4$ nm; (c) second peak (10 h AA), $t = 108.0$ nm. Notice the few "abnormally" long precipitates in (c). The red arrows indicate the ⟨100⟩ directions of Al.

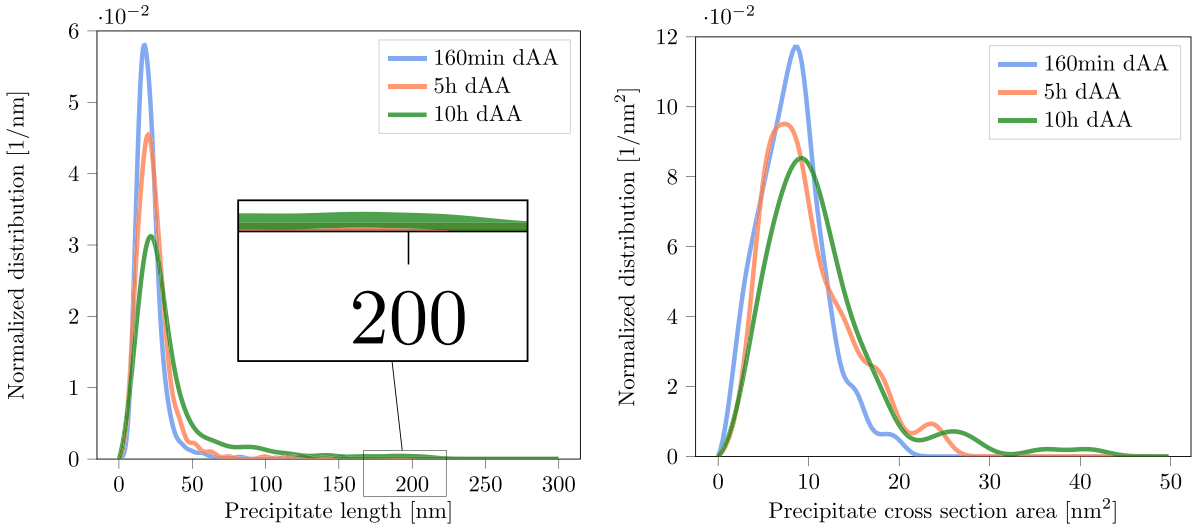


(a) (b)

**Fig. 4.** Precipitate length (a) and cross-sectional area (b) distributions for the first peak (160 min), between peaks (5 h) and second peak (10 h) conditions through kernel density estimates for the dAA treatment.

**Table 3**
Measured hardness values and estimated $R_p$ values. The conversion was done through: $R_p = 3 \cdot HV$.

| | dAA | | | rAA | | |
|---|---|---|---|---|---|---|
| | 160 min | 5 h | 10 h | 160 min | 5 h | 10 h |
| Measured HV [HV1] | 116.2 ± 4.4 | 113.4 ± 1.0 | 114.9 ± 3.5 | 109.6 ± 0.8 | 115.4 ± 2.3 | 115.0 ± 0.5 |
| Estimated Rp [MPa] | 348.6 ± 13.2 | 340.2 ± 3.0 | 344.7 ± 10.5 | 328.8 ± 2.4 | 346.2 ± 6.9 | 345.0 ± 1.5 |

**Table 4**
Summary of the precipitate type statistics of the six conditions from the dAA and rAA treatments. Example images for the different categories can be found in Fig. 1. Percentages may not total 100% due to rounding.

| | $\beta''_{perfect}$ | $\beta''_{hybrid}$ | L/C | B′ | Hybrid/post-$\beta''$ | Analyzed precipitates |
|---|---|---|---|---|---|---|
| dAA-160 min | 52.3% | 27.3% | – | 9.1% | 11.4% | 44 |
| dAA-5 h | 53.1% | 25% | 6.3% | 9.4% | 6.3% | 32 |
| dAA-10 h | 53.9% | 26.3% | 1.3% | 5.3% | 13.2% | 76 |
| rAA-160 min | 79.7% | 17.4% | – | – | 2.9% | 69 |
| rAA-5 h | 62.2% | 33.4% | – | 1.4% | 2.7% | 74 |
| rAA-10 h | 80.8% | 7.7% | – | 3.8% | 7.7% | 26 |

The three different heat treatments investigated in this study are too close in time to estimate reliably the parameters $c$ and $m$ for the $\Omega$ relation, which resembles the precipitate growth during AA, see Eq. (3). Instead, the slope of the fit curve $m = 0.74$ was adopted from Lu et al. [19] who analyzed a similar alloy, and suitable expressions for the $c$ values of the dAA and rAA were found by a least square fit : $c^{dAA} = 0.75$ and $c^{rAA} = 0.86$. The resulting $\sigma_p = M\tau_p$ estimates are summarized in Table 7.

The largest precipitates measured for the dAA treatment after 160 min AA is 152.1 nm in length. When omitting the precipitates that are longer than 160 nm from the strength estimation, the modeled double-peak of the dAA treatment disappears, see Table 8. However, in case of the rAA treatment no significant change in strength is calculated.

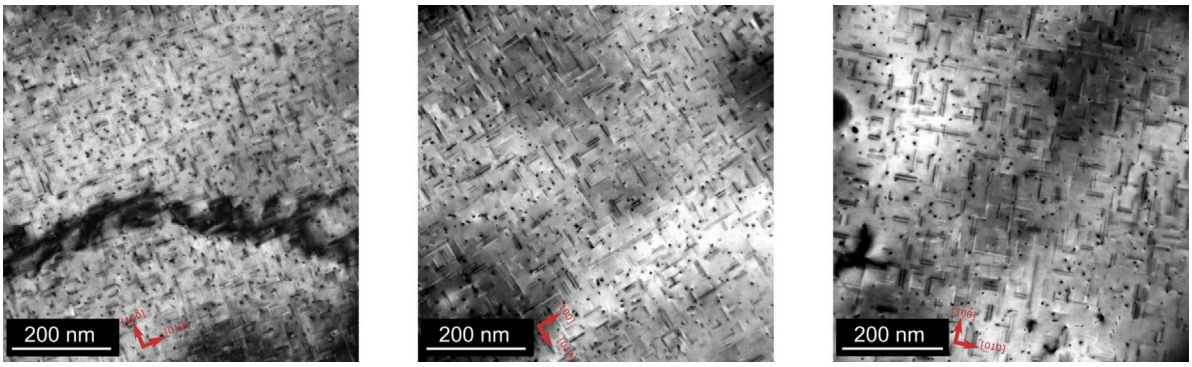


(a) 160 min (b) 5 h (c) 10 h

**Fig. 5.** One of the two images of the analyzed BF micrographs from each condition of the rAA treatment. The grains are [001] oriented and the corresponding thicknesses $t$ are given. (a) 160 min AA, $t = 84.6$ nm; (b) 5 h AA, $t = 46.4$ nm; (c) 10 h AA, $t = 44.7$ nm. The red arrows indicate the ⟨100⟩ directions of Al.

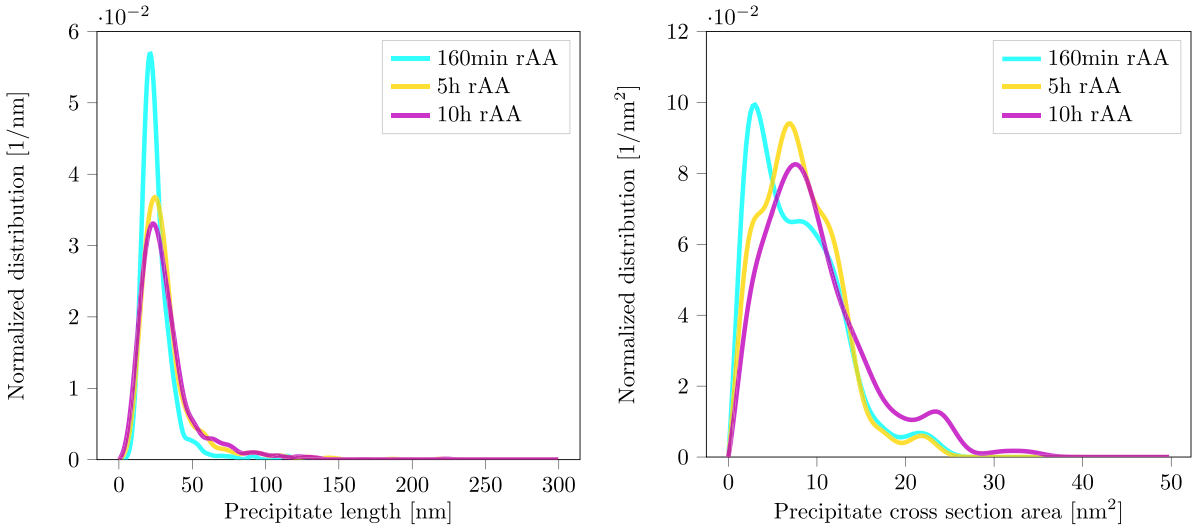


(a) (b)

**Fig. 6.** Precipitate length (a) and cross-sectional area (b) distribution of the 160 min, 5 h and 10 h conditions, through kernel density estimates for the rAA treatment with ramping up to the AA temperature.

**Table 5**
Summary of the precipitate statistics of the six analyzed conditions. The error margin, mean and peak values were acquired as mentioned earlier in the text.

| | $l_{mean}$ [nm] | $l_{Peak}$ [nm] | Meas. needles [#] | $\rho_{mean}$ [$\frac{\#}{nm^3}$] | $a_{mean}$ [nm$^2$] | Meas. cross sec. [#] | Vol. Frac. [%] |
|---|---|---|---|---|---|---|---|
| dAA-160 min | 21.4 ± 0.3 | 17.3 | 797 | $(9.2 \pm 0.7)10^{-5}$ | 8.2 ± 0.8 | 120 | 1.6 ± 0.14 |
| dAA-5 h | 24.1 ± 0.4 | 19.95 | 668 | $(6.9 \pm 1)10^{-5}$ | 9.9 ± 0.8 | 147 | 1.6 ± 0.24 |
| dAA-10 h | 36.2 ± 0.3 | 21.74 | 763 | $(5.0 \pm 0.3)10^{-5}$ | 11.3 ± 1.1 | 99 | 1.8 ± 0.10 |
| rAA-160 min | 25.7 ± 0.2 | 21.28 | 572 | $(6.3 \pm 0.9)10^{-5}$ | 7.05 ± 0.5 | 168 | 1.1 ± 0.17 |
| rAA-5 h | 31.95 ± 0.8 | 24.52 | 963 | $(5.7 \pm 0.6)10^{-5}$ | 7.64 ± 0.8 | 90 | 1.4 ± 0.15 |
| rAA-10 h | 31.97 ± 0.8 | 23.29 | 876 | $(5.2 \pm 0.5)10^{-5}$ | 9.25 ± 0.7 | 188 | 1.5 ± 0.14 |

**Table 6**
Summary of the input values for the strength calculations.

| $M$ | $G$ | $b$ | $\alpha_p^{dAA}$ | $\alpha_p^{rAA}$ | $a_c$ |
|---|---|---|---|---|---|
| 2.7 | 27 GPa | 0.286 nm | 0.602 | 0.632 | 7.6 nm$^2$ |

**Table 7**
Calculated $\sigma_p$ values.

| $\sigma_p$ [MPa] | 160 min | 5 h | 10 h |
|---|---|---|---|
| dAA | 348.5 | 320.3 | 338.3 |
| rAA | 319.6 | 346.4 | 331.0 |

**Table 8**
Calculated $\sigma_p$ values when only considering precipitate lengths smaller than 160 nm.

| $\sigma_p$ [MPa] | 160 min | 5 h | 10 h |
|---|---|---|---|
| dAA | 348.5 | 320.3 | 319.5 |
| rAA | 319.6 | 342.8 | 329.5 |

## 4. Discussion

In an earlier study we investigated the same heat treatments with this 6082 alloy and an additional Cu- containing 6110 alloy [14]. There, it was concluded that the ramp of the rAA treatment results in the formation of fewer potent precipitate nucleation sites, which during

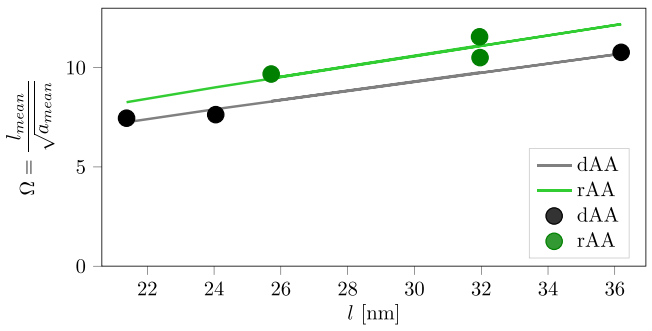


**Fig. 7.** The experimental mean aspect ratios $\Omega$ after different AA times of the dAA, and rAA heat treatments are compared to their expression of precipitate growth given by Eq. (3) with $m = 0.74$, $c^{dAA} = 0.75$ and $c^{rAA} = 0.86$.

the isothermal AA treatment result in an overall reduced precipitate number density of longer and purer precipitates that follow closer the precipitation sequence, e.g. less hybrid-type or $B'$-type precipitates during the rAA treatment. A higher amount of solute atoms in solid solution was found for rAA sample compared to the dAA sample by atom probe tomography and a shorter strength plateau for the ramped treatments was reported. Those results agree with the present study. A reduced $\rho_{mean}$ and an increased $l_{mean}$ were measured for all conditions of the rAA treatment compared to the dAA treatment. Additionally, more of the $\beta''_{perfect}$ precipitates and less of the $B'$ precipitates were found during the rAA conditions, as compared to the corresponding dAA conditions. In that way, the earlier findings of the effect on a ramp were re-affirmed in the present study also for the new analyzed conditions. In this study, however, we are interested in understanding why the microstructure of the dAA heat treatment results in a double-peak in the hardness curves, hence a broader strength plateau. We use the term double peak in the title to emphasize the two distinguishable contributions to each end of the extended strength plateau, i.e. a high number density of strong precipitates at the first peak and a lower density of slightly coarsened with some significantly longer needles at the second peak. However, the two "peaks" are blur with an overlap and cannot necessarily be well distinguished. Hence, we balance this description by the term "broader strength plateau".

### 4.1. Precipitate based strength modeling

On the basis of the estimated $R_p$ values from Table 3, the scaling parameter $\alpha_p$ was found. Note that the parameter $\alpha_p$ in Eq. (6) can vary from alloy to alloy and between different heat treatment routes, as it depends on the dislocation line tension and the dislocation core energies, which again depend on the stress and obstacle configurations, see Anderson et al. [30]. An upper estimate based on the line tension of a straight line would give $\alpha_p = 1$. A value is pragmatically derived by calibrating to the estimated peak strength of the treatment. The value $\alpha_p^{dAA} = 0.602$ is in the expected range. For the rAA treatment the value $\alpha_p^{rAA} = 0.632$ was found.

To apply the strength model, a suitable expression for $\Omega(l) = c * l^m$ – which models the precipitate growth – needs to be found. This is ideally done by measuring the changes of $l_{mean}$ and $a_{mean}$ over a wide span of different AA times and finding an adequate fit for Eq. (3). In this work only three conditions per heat treatment were analyzed over a relatively short AA span. Fig. 7 shows that the calibration of the slope $m$, based on the earlier work by Lu et al. [19], provides a suitable fit within the spread of the data. That work was based on a precipitate statistics acquired in a similar manner of another 6082 artificially aged at 180 °C. To fit Eq. (3) to the data points of the current work, the correct intercept $c$ had to be found by a least square fit. For the two analyzed heat treatments, this value was found to be $c^{dAA} = 0.75$ and $c^{rAA} = 0.86$. The difference in $c$ gives a difference in the critical precipitate length $l_c$ which expresses the length at which the critical cross section $a_c$ is reached, thus when the particles contribute with a maximum obstacle strength $f = 1$ and the transition from shearing to looping occurs. The calculated critical lengths of the two treatments are $l_c^{dAA} = 16.3$ nm and $l_c^{rAA} = 27.7$ nm, respectively. The mean obstacle strengths $\bar{f}$ at peak strength is higher for the dAA treatment compared to the rAA treatment. Furthermore, $\bar{f}$ of the dAA treatment is continuously increasing between the conditions until it reaches unity after 10 h AA. On the other hand, the mean obstacle strength of the rAA treatment reaches its maximum after 5 h AA. The number density of precipitate-based obstacles per slip plane $n_p$ is noticeable lower for the rAA treatment, as well. The relatively low $\bar{f}$ values of the rAA treatment comes from the relatively large $l_c$ value which lies above the $l_{Peak}$ values of all three conditions. Thus, many of the measured precipitates do not act as obstacles of high strength. The values for the different $l_c$, $n_p$ and $\bar{f}$ can be found in Tables 9 and 10.

When comparing the trend of the calculated strength values from Table 7 with the values from Table 3, one sees that the double-peak of the dAA treatment, which should rather be seen as a broader strength plateau, as well as the single peak of the rAA treatment, are well reflected in the modeled data, see Table 7.

*The influence of choosing the critical precipitate cross section area on the double-peak*

Choosing an adequate value for a critical precipitate size above which looping sets in, is alloy dependent and thus no definite value exists. Hu and Curtin [31] showed that the same precipitate could either be sheared or looped, depending on its orientation with respect to the gliding dislocation. Furthermore, they showed the critical radius can be found close to peak strength. Nie et al. [12] argue that the transition to particle bypassing may occur still in the underaged state. We declared the smallest average cross sectional area found at peak strength as the critical cross section $a_c$. However, choosing different values as $a_c$ has little consequence on modeling the actual double-peak, as long the value chosen is not unrealistically large, e.g. larger than the majority of the measured cross-sections. Table 11 shows the influence of the critical cross section on the different conditions of the dAA route. It can be seen, that an increase of the critical cross section increases the value of the critical length $l_c$ which defines, through Eq. (5), when a precipitate is thick enough to withstand shearing. Consequently, the calculated $\sigma_p$ values decrease, most notably for the condition after 160 min AA. As a result, the peak strength is shifted from the 160 min condition to the 10 h condition. However, in the experimental data the 160 min dAA condition shows the peak hardness, thus peak strength, see Table 3. That the first peak gives higher hardness values is commonly found in literature as well [3,13,32].

### 4.2. The origin of the double-peak in the dAA treatment

To the authors knowledge, no study dealing with the double-peak behavior in age hardening metallic systems has been able to model the double-peak solely on the basis of experimental data. Most of the work published on this topic are thus based on finding a certain precipitate type to explain the double-peak behavior [3,10,11], or on changing pre-existing strength models to account for double-peak aging by introducing extra fit parameters [12,33]. Since the here applied model managed to reproduce the hardness curve of the analyzed conditions for the two different heat treatments sufficiently well, the results of the model can be used to explore the origin of the double-peak behavior, i.e. the broader strength plateau.

The results of the precipitate type study in this work do not show evidence that any of the strength peaks can be attributed to a certain precipitate type. In fact, the precipitate type analysis suggests that during the peak-strength plateau of the dAA treatment no significant

**Table 9**
Calculated data from the strength modeling of the dAA treatment.

| | $l_c$ [nm] | 160 min | | 5 h | | 10 h | |
|---|---|---|---|---|---|---|---|
| | | $\bar{f}$ | $n_p$ | $\bar{f}$ | $n_p$ | $\bar{f}$ | $n_p$ |
| Considering all measured precipitates | 16.3 | 0.981 | 0.00113 | 0.984 | 0.00095 | 1.000 | 0.00105 |
| Considering precipitates < 160 nm | 16.3 | 0.981 | 0.00113 | 0.984 | 0.00095 | 0.998 | 0.00094 |

**Table 10**
Calculated data from the strength modeling of the rAA treatment.

| | $l_c$ [nm] | 160 min | | 5 h | | 10 h | |
|---|---|---|---|---|---|---|---|
| | | $\bar{f}$ | $n_p$ | $\bar{f}$ | $n_p$ | $\bar{f}$ | $n_p$ |
| Considering all measured precipitates | 27.7 | 0.930 | 0.00094 | 0.957 | 0.00105 | 0.957 | 0.00096 |
| Considering precipitates < 160 nm | 27.7 | 0.930 | 0.00094 | 0.930 | 0.00105 | 0.956 | 0.00095 |

**Table 11**
Calculated $\sigma_p$ values for the different conditions of the dAA treatment with different $a_c$ values but a constant $\alpha_p = 0.602$.

| $a_c$ [nm$^2$] | $l_c$ [nm] | 160 min [MPa] | 5 h [MPa] | 10 h [MPa] |
|---|---|---|---|---|
| 7.1 | 14.3 | 350.4 | 321.5 | 338.3 |
| 7.6 | 16.3 | 348.5 | 320.3 | 338.3 |
| 9.9 | 27.2 | 319.0 | 302.5 | 333.7 |
| 15.0 | 60.4 | 207.5 | 208.8 | 286.7 |

change in precipitate type occurrence appears. The precipitate cross-sectional area distributions from the dAA treatment of Fig. 4(b) and the even increase of the $l_{Peak}$ and $a_{mean}$ values support those observations and indicate that the majority of the precipitates are gradually growing during the AA process from 160 min to 10 h, both in terms of lengths and thicknesses.

The output of the strength modeling, i.e. the resulting critical length for looping $l_c$, the mean obstacle strength $\bar{f}$ and the number density of precipitate-based obstacles per slip plane $n_p$, are given in Table 9 for the dAA treatment and in Table 10 for the rAA treatment. According to the model, the mean obstacle strength $\bar{f}$ increases for the dAA heat treatments until it reaches unity after around 10 h of AA. The $n_p$ value on the other hand, decreases between 160 min and 5 h AA, just to rise again after 10 h AA. Thus, its course resembles a double-peak. The longest precipitate measured in the dAA treatment after 160 min AA is 152.1 nm. After 10 h AA a small population of precipitates with a length of about 200 nm has emerged, see the inset in Fig. 4(a). Additionally to that, a broad peak in the cross-sectional area distribution at about 40 nm$^2$ has emerged after 10 h, refer to Fig. 4(b). It is reasonable to assume that the extra peaks in the length and cross-sectional area distributions belong to the same population of precipitates, thus, that the relative wide precipitates are long, as well. To analyze the importance of the presence of the longest particles formed after 10 h AA, it is interesting to exclude them from the strength estimation. Their exclusion reduces the $l_{mean}$ after 10 h AA to 32.4 nm and lowers $\bar{f}$ and $n_p$ to 0.998 and 0.00094, respectively. Without considering the long precipitates, $n_p$ is now steadily decreasing for the three investigated AA times, while $\bar{f}$ is still increasing. The double-peak in strength of the dAA treatment, however, disappears, see Table 8. The origin of the double-peak lies, thus, in the few excluded precipitates. These long and presumably wide precipitates can act as dislocation obstacles for a high number of dislocations each – taken into account by the increase of $n_p$ – and are playing an important role in maintaining the strength of the alloy. Their exclusion demonstrates the strong effect that the 18 longest precipitates – about 2.4% of all measured ones – can have on the final strength.

The rAA treatment does not show a double-peak of strength during the age hardening. The reason for this is two-fold: The decrease of the precipitate number density from Ostwald ripening is not counter-acted by an increase in length and thus an increase of $n_p$. Additionally, the rAA treatment produces rather slim and therefore weak precipitates. This results in the relatively large critical length $l_c^{rAA}$. As a consequence, the precipitates need to grow longer before they reach the maximum obstacle strength. This leads to the lower mean obstacle strength $\bar{f}$ of the precipitates after 160 min rAA and to reaching later the peak strength. Table 8 shows that considering only precipitates up to 160 nm has basically no effect on the resulting $\sigma_p$ values. This is because in the analyzed micrographs of the rAA treatment only two precipitates longer than 160 nm were measured after 5 h AA and only one precipitate was measured after 10 h AA. Their exclusion has a negligible effect on the strength estimation.

The broader strength plateau due to a double-peak is thus the result of having many already fairly wide, and hence strong, particles early on and the co-existence of some significantly longer and thus potent dislocation obstacles at later times. The few long precipitates compensate the effect of Ostwald ripening. That the precipitates are wider in cross section after the dAA heat treating route stems from the higher occurrence of B′, hybrid/post-$\beta''$ and $\beta''_{hybrid}$ phases [14].

### 4.3. A closer look at the large precipitates of the dAA treatment

It is interesting to discuss why the dAA treatment produces such potent long and presumably wide precipitates. As mentioned earlier, (S)TEM does not allow to image the length and the cross section of the same precipitate. Thus, one has to draw conclusions from acquired size distributions. The cross sectional area distribution of the precipitates after 10 h AA of the dAA treatment is shown in Fig. 4(b). That distribution has two dominant peaks at 9.2 nm$^2$ and 26.0 nm$^2$, as well as, one broad one consisting of two overlapping peaks at 36.4 nm$^2$ and 40.6 nm$^2$. The corresponding distribution of the rAA treatment consists of only three peaks at 7.6 nm$^2$, 23.4 nm$^2$ and 32.2 nm$^2$, see Fig. 4(b). We assume that precipitates after 10 h dAA larger than 30.0 nm$^2$ measured from HAADF-STEM micrographs can be attributed to the broad peak. Imaging exclusively such large precipitates of the 10 h dAA condition revealed that they are of no specific precipitate type. Fig. 8 shows distortion corrected HAADF-STEM micrographs of such large precipitates. All the cross sections show a mixed precipitate character with a high occurrence of overaged phases, i.e. $\beta'$, $B'$ and $U2$ building blocks, supporting the observation of no specific precipitate type being present. Overaged precipitates are known to be large in size [19,20]. It can thus be assumed that those wide precipitates are long, as well.

According to the inset from Fig. 4(a), the long precipitates of the dAA treatment have lengths at around 190 nm. From Eq. (3) with the fit-parameters from Fig. 7 the model yields an aspect ratio of around $\Omega = 36.4$, hence a cross-section of around $a = 27.2$ nm$^2$ can be expected for these long precipitates. The cross-sectional size distribution from Fig. 4(b) suggests that the long precipitates have cross-sections at around 38.5 nm$^2$, which would give an aspect ratio of $\Omega = 30.6$ for 190 mn long precipitates. It can be seen that the model, in spite of all its simplifications, predicts the aspect ratios for the long precipitates reasonably well. However, determining the correct aspect ratio of non-shearable precipitates is not a critical step for the strength estimation.

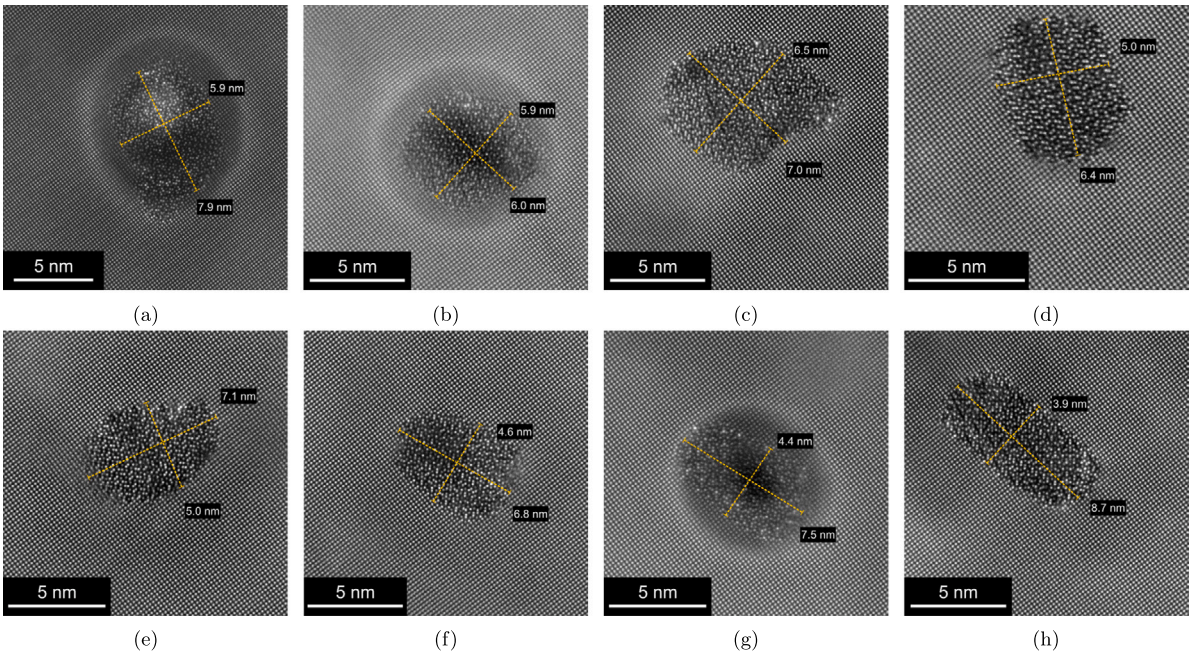


**Fig. 8.** Micrographs from the 10 h dAA condition. The images show precipitates with a cross sectional area larger than $30\,nm^2$. The precipitates are all of an hybrid type and show structures of different phases, mostly of $\beta'$, B′ and U2. The extensions of their dominant axes is shown.

As long as the particles are sufficiently thick, they will contribute with a particle strength of $f = 1$ to Eq. (8).

The next question is then why does the dAA produce a significant amount of post-$\beta''$ phases which can contribute to the strength, whereas the rAA treatment does not?

Not much attention has been given in literature to the heating rate prior to AA which is the only difference in the two discussed heat treatments. The results of the present study can thus not be directly compared to the work of others. Similar findings were, however, made by Li et al. [13]. They found by tensile tests that the occurrence of a double-peak in strength in age hardenable cast Al–Si base alloys can be provoked by aging the alloys at AA temperatures above 145 °C. When aging at 145 °C, the alloy reaches a higher peak strength value, as expected, but no double-peak in strength was observed. A low AA temperature of 145 °C results in a slower sample heat-up compared to their other AA temperatures, e.g. 185 °C or 215 °C, which showed a pronounced double-peak. Hell et al. [14] discussed the here applied heat treatments for this Cu lean 6082 and another Cu containing 6110. The 6110 did not produce a double-peak, but ramping the 6110 still led to a narrower strength plateau in the hardness curves, together with an increased occurrence of longer and purer precipitates. In that study it was concluded that the high rate of heating of the dAA treatment leads early on to the formation of the thermodynamically more stable post-$\beta''$ structures, thus hybrid-type precipitates. On the other hand, a restricted heat feed through a ramp forces the system to follow closer along the precipitation sequence resulting in the formation of less post-$\beta''$ structures. The same was also observed in the precipitate type analysis in Table 4. The dAA treatment showed more hybrid, B′ and $\beta''_{Hybrid}$ phases in all analyzed conditions compared to the rAA treatment. Thus, wider average cross sections were measured for the dAA route. It seems therefore, that by introducing some post-$\beta''$ structures early on, the formation of hybrid phases can be promoted at later AA times which in turn can contribute to maintaining the strength due to the large size they may reach.

The alloys of the studies by Saito et al. [3] and Mørtsell et al. [32] showed a comparable double-peak as the one of this work. Mørtsell et al. [32] saw in foundry alloys that the addition of Cu provokes the double-peak. The addition of Cu is known to result in an increased precipitate number density, as well as, in the creation of more hybrid precipitates [2]. Thus, the reason for the double-peak observed in that study might be similar to the one analyzed and discussed here. In the work by Saito et al. [3] a similar double-peak was observed in two treatments that experienced a deformation prior to AA. The introduction of dislocations through pre-deformation accelerates diffusion processes thus leads to more overaged structures, as well.

## 5. Conclusion

In this study three conditions of two different heat treatment routes, with and without a temperature ramp up to the artificial aging temperature, were characterized by (S)TEM, hardness measurements and strength modeling to explore the microstructural origin of a double-peak in the hardness curves. Without the temperature ramping, the peak strength sets in earlier, with a first strength peak after 160 min artificial aging and the second after around 10 h. The precipitate structure of the first peak consists of a higher number density of wider precipitates with shorter lengths. Based on strength estimates that account for number density, size distribution and the high aspect ratio shape of the individually measured precipitates, it can be concluded that the second peak arises from the formation of some few but unusually long precipitates. Due to their large size, they can pin dislocations more efficiently than the shorter ones and counteract the strength decay from Ostwald ripening. Those precipitates were found to be of no specific type, but they all posses structures of several different overaged phases.

With the ramp, this broad strength plateau does not occur. Peak strength is only reached after 5 h AA and a strength loss sets in afterwards. The slower heating to artificial aging temperature results in on average longer but slimmer and fewer precipitates.

Those distinct differences of the microstructures were related to the different kind of phases which emerged from the two different heat treatments. Due to the rapid heat-up of the dAA treatment, structures of overaged phases have emerged within the precipitates. Therefore, wider, thus, stronger precipitates formed after 160 min AA and some long overaged hybrids were present after 10 h AA. The ramp resulted in the formation of more of the longer and typically leaner $\beta''_{perfect}$ precipitates

## Declaration of competing interest

The authors declare that they have no known competing financial interests or personal relationships that could have appeared to influence the work reported in this paper.

## Acknowledgments

Benteler Automotive Raufoss AS (Ynge Langsrud and Lars Lodgaard) is acknowledged for providing the material for this study. This work was supported by the The Research Council of Norway (NFR) through the project 'SumAl' (NFR: 294933), supported by Hydro, Benteler Automotive Raufoss AS, Speira and Neuman Aluminium. The (S)TEM work was conducted on the NORTEM (NFR: 197405) infrastructure at the TEM Gemini Centre, Trondheim, Norway. We would like to thank head engineer Pål Christian Skaret for helping with the mechanical tests.

## Appendix A. Supplementary data

Supplementary material related to this article can be found online at https://doi.org/10.1016/j.actamat.2023.119095.

## References

[1] B. Holmedal, Strength contributions from precipitates, Phil. Mag. Lett. (ISSN: 13623036) 95 (12) (2015) 594–601, http://dx.doi.org/10.1080/09500839.2015.1125029.

[2] T. Saito, E.A. Mørtsell, S. Wenner, C.D. Marioara, S.J. Andersen, J. Friis, K. Matsuda, R. Holmestad, Atomic structures of precipitates in Al–Mg–Si alloys with small additions of other elements, (ISSN: 15272648) 20 (7) (2018) 1800125. http://dx.doi.org/10.1002/adem.201800125.

[3] T. Saito, C.D. Marioara, J. Røyset, K. Marthinsen, R. Holmestad, The effects of quench rate and pre-deformation on precipitation hardening in Al-Mg-Si alloys with different cu amounts, Mater. Sci. Eng. A (ISSN: 09215093) 609 (2014) 72–79.

[4] S. Pogatscher, H. Antrekowitsch, H. Leitner, T. Ebner, P.J. Uggowitzer, Mechanisms controlling the artificial aging of Al-Mg-Si alloys, Acta Mater. (ISSN: 13596454) 59 (9) (2011) 3352–3363, http://dx.doi.org/10.1016/j.actamat.2011.02.010.

[5] C.D. Marioara, S.J. Andersen, T.N. Stene, H. Hasting, J. Walmsley, A.T. Van Helvoort, R. Holmestad, The effect of cu on precipitation in Al-Mg-Si alloys, Phil. Mag. (ISSN: 14786435) 87 (23) (2007) 3385–3413.

[6] G. Gottstein, Physical Foundations of Materials Science, ISBN: 9783642072710, 2004.

[7] W. Poole, X. Wang, D. Lloyd, J. Embury, The shearable–non-shearable transition in Al–Mg–Si–Cu precipitation hardening alloys: implications on the distribution of slip, work hardening and fracture, Phil. Mag. 85 (26–27) (2005) 3113–3135.

[8] D. Porter, K. Easterling, M.Y. Sherif, Phase transformations in metals and alloys, 2009.

[9] E.V. Pereloma, A. Shekhter, M.K. Miller, S.P. Ringer, Ageing behaviour of an Fe-20Ni-1.8Mn-1.6Ti-0.59Al (wt%) maraging alloy: Clustering, precipitation and hardening, Acta Mater. (ISSN: 13596454) 52 (19) (2004) 5589–5602.

[10] Y.L. Zhao, Z.Q. Yang, Z. Zhang, G.Y. Su, X.L. Ma, Double-peak age strengthening of cold-worked 2024 aluminum alloy, Acta Mater. (ISSN: 13596454) 61 (5) (2013) 1624–1638.

[11] C.D. Marioara, S.J. Andersen, H.W. Zandbergen, R. Holmestad, The influence of alloy composition on precipitates of the Al-Mg-Si system, Metall. Mater. Trans. A: Phys. Metall. Mater. Sci. (ISSN: 10735623) 36 (13) (2005) 691–702.

[12] X.W. Nie, L.J. Zhang, Y. Du, Experiments and modeling of double-peak precipitation hardening and strengthening mechanisms in Al-Zn-Mg alloy, Trans. Nonferrous Metals Soc. China (Engl. Ed.) (ISSN: 10036326) 24 (7) (2014) 2138–2144, http://dx.doi.org/10.1016/S1003-6326(14)63324-0.

[13] R.X. Li, R.D. Li, Y.H. Zhao, L.Z. He, C.X. Li, H.R. Guan, Z.Q. Hu, Age-hardening behavior of cast Al-Si base alloy, Mater. Lett. (ISSN: 0167577X) 58 (15) (2004) 2096–2101.

[14] C.M. Hell, H.-S. Søreide, R. Bjørge, C.D. Marioara, Y. Li, R. Holmestad, Influence of natural aging and ramping before artificial aging on the microstructure of two different 6xxx alloys, J. Mater. Res. Technol. 21 (2022) 4224–4240.

[15] L. Jones, H. Yang, T.J. Pennycook, M.S. Marshall, S. Van Aert, N.D. Browning, M.R. Castell, P.D. Nellist, Smart align—a new tool for robust non-rigid registration of scanning microscope data, Adv. Struct. Chem. Imaging (ISSN: 21980926) 1 (1) (2015) 1–16, http://dx.doi.org/10.1186/s40679-015-0008-4.

[16] C.M. Hell, CBED ThicknessDeterminationTEM, 2022, http://dx.doi.org/10.5281/zenodo.6602265.

[17] O.R. Myhr, O. Grong, S.J. Andersen, Modelling of the age hardening behaviour of Al-Mg-Si alloys, Acta Mater. (ISSN: 13596454) 49 (1) (2001) 65–75.

[18] U.F. Kocks, A.S. Argon, M.F. Ashby, Thermodynamics and kinetics of slip, 1975.

[19] F. Lu, J.K. Sunde, C.D. Marioara, R. Holmestad, B. Holmedal, An improved modelling framework for strength and work hardening of precipitate strengthened Al–Mg–Si alloys, Mater. Sci. Eng. A (ISSN: 09215093) 832 (December 2021) (2021) 142500.

[20] Q. Du, B. Holmedal, J. Friis, C.D. Marioara, Precipitation of non-spherical particles in aluminum alloys part II: numerical simulation and experimental characterization during aging treatment of an Al-Mg-Si alloy, Metall. Mater. Trans. A 47 (2016) 589–599.

[21] S. Esmaeili, D. Lloyd, W. Poole, A yield strength model for the Al-Mg-Si-Cu alloy AA6111, Acta Mater. 51 (8) (2003) 2243–2257.

[22] L. Cheng, W. Poole, J. Embury, D. Lloyd, The influence of precipitation on the work-hardening behavior of the aluminum alloys AA6111 and AA7030, Metall. Mater. Trans. A 34 (11) (2003) 2473–2481.

[23] A. De Vaucorbeil, W.J. Poole, C.W. Sinclair, The effect of obstacle strength distribution on the critical resolved shear stress of engineering alloys, Mater. Sci. Forum (ISSN: 16629752) 794–796 (2014) 449–454,

[24] H.E. Boyer, T.L. Gall, Metals handbook; desk edition, 1985, https://www.osti.gov/biblio/5760918.

[25] W.D. Callister, D.G. Rethwisch, et al., Materials Science and Engineering: An Introduction, Vol. 7, John Wiley & Sons New York, 2007.

[26] L. Lu, R. Schwaiger, Z. Shan, M. Dao, K. Lu, S. Suresh, Nano-sized twins induce high rate sensitivity of flow stress in pure copper, Acta Mater. 53 (7) (2005) 2169–2179.

[27] H. Li, F. Ebrahimi, Synthesis and characterization of electrodeposited nanocrystalline nickel–iron alloys, Mater. Sci. Eng. A 347 (1–2) (2003) 93–101.

[28] P. Sanders, C. Youngdahl, J. Weertman, The strength of nanocrystalline metals with and without flaws, Mater. Sci. Eng. A 234 (1997) 77–82.

[29] K. Zhang, B. Holmedal, T. Mánik, A. Saai, Assessment of advanced taylor models, the taylor factor and yield-surface exponent for FCC metals, Int. J. Plast. (ISSN: 0749-6419) 114 (2019) 144–160, https://www.sciencedirect.com/science/article/pii/S0749641918301980.

[30] P.M. Anderson, J.P. Hirth, J. Lothe, Theory of Dislocations, Cambridge University Press, 2017.

[31] Y. Hu, W.A. Curtin, Modeling of precipitate strengthening with near-chemical accuracy: case study of Al-6xxx alloys, Acta Mater. (ISSN: 13596454) 237 (2022).

[32] E.A. Mørtsell, F. Qian, C.D. Marioara, Y. Li, Precipitation in an A356 foundry alloy with Cu additions - A transmission electron microscopy study, J. Alloys Compd. (ISSN: 09258388) 785 (2019) 1106–1114, http://dx.doi.org/10.1016/j.jallcom.2019.01.229.

[33] H. Fan, A.H. Ngan, K. Gan, J.A. El-Awady, Origin of double-peak precipitation hardening in metallic alloys, Int. J. Plast. (ISSN: 07496419) 111 (March) (2018) 152–167, http://dx.doi.org/10.1016/j.ijplas.2018.07.016.